Numerical Heat Transfer, Part B, 37:489–508, 2000

1040–7790/00 $12.00 + .00

FLOW AND HEAT TRANSFER IN RECTANGULAR ENCLOSURES USING A NEW BLOCK-IMPLICIT NUMERICAL METHOD

Marcelo J. S. de Lemos
Departamento de Energia, IEME, Instituto Tecnológico de Aeronáutica, ITA, 12228-900 São José dos Campos, São Paulo, Brasil

This work reports a numerical investigation on buoyancy-induced flows occurring in enclosures of small aspect ratio and inclined with respect to the horizontal direction. The numerical method used consists of the control-volume approach and a new block-implicit error-smoothing operator. Governing equations are written in terms of primitive variables and are recast into a general form. In the proposed method, all governing equation are relaxed locally, in contrast with commonly used segregated schemes. The effects of Rayleigh number, aspect ratio, and cavity inclination on temperature and velocity patterns are discussed. It is expected that more advanced parallel computer architectures can benefit from the error-smoothing operator described here.

INTRODUCTION

The problem of heat transfer enhancement through gaps between walls in cavities finds many applications in science and engineering [1, 2]. Enhancement or damping of heat transfer rates across layers of fluids have a wide range of employment, from simple insulating systems to sophisticated technological devices [3]. When the system is closed and subjected to a temperature gradient, a recirculating flow field is established. If the cavity itself is further inclined with respect to the vertical direction, important changes occur in the heat transfer strength across the domain [4].

For two-dimensional cases, in addition to having gravity directly affecting both coordinates, the numerical solution of such flows imposes additional difficulties due to the intricate coupling between *temperature* and *cross-flow* fields. Linearization of governing equations followed by the use of iterative solvers is the common route found in the literature for solving such nonlinear problems. Accordingly, the rate of convergence of any algorithm is essentially dictated by the degree in which physical coupling is mimicked by the method in question. Ultimately, this is an indication that numerical solutions of buoyant flows, in most cases, suffer from the disadvantage of longer computing times when compared to their non-buoyant counterpart.

Received 10 August 1999; accepted 15 October 1999.
The author is thankful to CNPq, Conselho Nacional de Desenvolvimento Científico e Tecnológico, Brazil, for their financial support during the preparation of this work.
Address correspondence to Prof. Marcelo J. S. de Lemos, Departamento de Energia, IEME, Instituto Tecnológico de Aeronáutica, ITA, 12228-900 São José dos Campos, São Paulo, Brazil. E-mail: mdelemos@tecsat.com.br

NOMENCLATURE

a–g	coefficients in the finite-volume equations
A_{nb}	area of volume face associated with neighbor point in the grid
F	coefficients for continuity equation
F_{in}	total mass flux entering the control volume
F_{out}	total mass flux leaving the control volume
g	gravity acceleration
h	film coefficient
H	cavity height
k	fluid thermal conductivity
L	cavity width
M	number of cells in z direction
N	number of cells in y direction
Nu	Nusselt number
P	pressure
Pr	Prandtl number
R_{abs}	absolute residue for mass continuity equation
R_{rel}	relative residue for mass continuity equation
R_T	residue for energy equation
Ra	Rayleigh number
Re	Reynolds number
S_ϕ	source term for variable $\phi = U, W, T$
T	temperature (T_1 = hot wall temp., T_0 = cold wall temp.)
U	velocity component in y direction
W	velocity component in z direction
y	coordinate along cavity width L
z	coordinate along cavity height H
α	cavity tilt angle
β	fluid thermal expansion coefficient
γ_ϕ	relaxation parameter for $\phi = U, W, P, T$
Γ_ϕ	transport coefficient for variable $\phi = U, W, T$
δr_{nb}	distance between nodal and neighbor points in the grid
ΔT	temperature drop across cavity width L ($= T_1 - T_0$)
Θ	nondimensional temperature: $[= (T - T_0)/(T_1 - T_0)]$
μ	fluid dynamic viscosity
ρ	fluid density
ϕ	general dependent variable, $(= U, W, \Theta)$

Subscripts

abs	absolute
rel	relative
ϕ	referent to general dependent variable
i, j	nodal indices for volume centered variables
$i - 1/2$, $j - 1/2$	indices for volume faces
0	cold wall, reference value
1	hot wall
T	temperature
nb	neighbor

Segregated methods, in which one individual flow variable is relaxed while holding the others still, are known to be rather sensitive when handling strong physical coupling. For that, the so-called *coupled* solvers, where all dependent variables are relaxed in the same domain location, have received much attention lately.

Benchmark solutions for the buoyancy-driven laminar flow field in a square cavity have been presented [5], and a comparison of 37 different contributions for solving the same problem has been compiled by the same author [6]. A multigrid solution for this problem has also been published [7]. In the great majority of those works a segregated method is generally employed, with the repetitive solution of a pressure or pressure-correction equation followed by subsequent updates of the velocity and scalar fields. This strategy forms the basis of the SIMPLE family of algorithms [8]. Coupled line solvers for the temperature and velocity fields have shown improvements in computer time requirements for natural-convection flows with large Rayleigh numbers [9]. The work in [9] is an indication of the advantage

of coupled schemes for solving algebraic equations set with a high degree of interlinkage among the variables. Recently, the block-implicit technique has also been applied to calculation of buoyant flows in a partially coupled manner [10]. In the present context, a fully implicit treatment is associated with the idea of simultaneously updating flow and temperature fields at each step within the error-smoothing operator. To the best of the author's knowledge, in none of the published work is the temperature field treated in a fully implicit manner.

Following the aforementioned and based on Vanka's SGCS method [11, 12], simulated lid-driven cavity fluid motion using a block-implicit numerical scheme was presented in [13]. Later, the technique was extended to buoyancy-driven streams [14], including vertical [15] and inclined cavities [16]. In those articles, a fully implicit treatment for temperature was made use of. The objective of this work is to present the numerical formulation extending the block-implicit arrangement to include a fully implicit treatment of the energy equation [13–16]. Heat cavity flows for vertical, horizontal, and inclined geometry with respect to the horizontal direction are presented. Effects of tilt angle, Rayleigh number, and aspect ratio are reported.

ANALYSIS AND NUMERICS

Geometry

The geometry considered in this work is shown schematically in Figure 1. An enclosure of height H and width L is insulated at both the top and bottom walls, while constant-temperature conditions T_1 and T_0 prevail over its lateral faces,

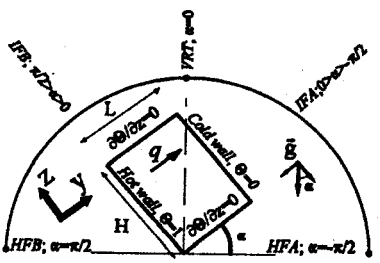

Geometry and boundary conditions

(*a*)

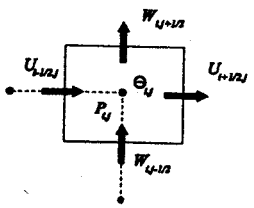

Control-volume notation

(*b*)

Figure 1. Geometry and general notation.

Table 1. Cases investigated

Case	Angle α	Description
HFB	$\pi/2$	Horizontal, heated from below
IFB	$\pi/2 < \alpha < 0$	Inclined, heated from below
VRT	$\alpha = 0$	Vertical, heated from left
IFA	$0 < \alpha < -\pi/2$	Inclined, heated from above
HFA	$-\pi/2$	Horizontal, heated from above

respectively. Depending on the value of tilt angle α, several cases can be identified as in Table 1. Cases in the table are referred to in Figure 1.

Compact Notation

The conservation equations for mass, momentum, and energy analyzed here can be written in a compact form if the existing analogies among the processes of accumulation, transport, convection, and generation/destruction of those quantities are observed. This generic equation is commonly known in the literature as the *general transport equation* and can be written in its *conservative* two-dimensional laminar form as

$$\frac{\partial}{\partial x_j}\left(\rho U_j \phi - \Gamma_\phi \frac{\partial \phi}{\partial x_j}\right) = S_\phi \tag{1}$$

In Eq. (1), ϕ can represent any quantity of vectorial or scalar nature (velocity or temperature), ρ is the fluid density, U_j are the velocity components (U, W) in the x_j directions (y, z), respectively, Γ_ϕ is the transport coefficient for diffusion, and S_ϕ is the source term. Table 2 identifies correspondent terms for the different equations represented by Eq. (1). In Table 2 and Eq. (1), gravity acts in both the z and y directions, μ is the fluid viscosity, Pr is the Prandtl number, and T is the temperature.

Table 2. Terms in the transport equation

	ϕ	Γ_ϕ	S_ϕ
Continuity	1	0	0
z Momentum	W	μ	$-\dfrac{\partial P}{\partial z} - \cos\alpha\, \rho_0 g \beta (T - T_0)$
y Momentum	U	μ	$-\dfrac{\partial P}{\partial y} - \sin\alpha\, \rho_0 g \beta (T - T_0)$
Energy	T	μ/Pr	0

Discretized Equations

The set of equations for mass, momentum, and energy summarized above is *differentiated* by means of the widely used control-volume approach of Patankar, 1980 [8]. Equation (1) is integrated over the volume of Figure 1, yielding a set of algebraic equations. In the present work, for simplicity, the *upwind differencing scheme* is used to model convective fluxes across volume faces.

Integrating, then, the continuity, momentum, and energy equations around point (ij) (see notation on Figure 1), one has

$$F_{i+1/2}U_{i+1/2,j} - F_{i-1/2}U_{i-1/2,j} + F_{j+1/2}W_{i,j+1/2} - F_{j-1/2}W_{i,j-1/2} = 0 \quad (2)$$

$$U_{i-1/2,j} = \hat{U}_{i-1/2,j} + \hat{d}_{i-1/2}(P_{i-1,j} - P_{i,j}) + \hat{g}_{i-1/2}\Theta_{i,j} \quad (3)$$

$$W_{i,j-1/2} = \hat{W}_{i,j-1/2} + \hat{d}_{j-1/2}(P_{i,j-1} - P_{i,j}) + \hat{g}_{j-1/2}\Theta_{i,j} \quad (4)$$

where

$$\hat{U}_{i-1/2,j} = \left(\sum_{\text{nb}=1}^{4} a^u_{\text{nb}} U_{\text{nb}} + f^u_{i-1/2,j} \right) / a^u_{i-1/2,j} \quad (5)$$

$$\hat{W}_{i,j-1/2} = \left(\sum_{\text{nb}=1}^{4} a^w_{\text{nb}} W_{\text{nb}} + f^w_{i,j-1/2} \right) / a^w_{i,j-1/2} \quad (6)$$

$$\Theta_{i,j} = \hat{\Theta}_{i,j} = \left\{ \sum_{\text{nb}=1}^{4} a^{\Theta}_{\text{nb}} \Theta_{\text{nb}} \right\} / a^{\Theta}_{i,j} \quad (7)$$

and

$$\hat{d}_{i-1/2} = \frac{S^u_{i-1/2}}{a^u_{i-1/2,j}}$$

$$\hat{g}_{i-1/2} = \frac{\rho_0 \sin \alpha g \beta (T_1 - T_0)}{2 a^u_{i-1/2,j}} \quad (8)$$

$$\hat{d}_{j-1/2} = \frac{S^w_{j-1/2}}{a^w_{i,j-1/2}}$$

$$\hat{g}_{j-1/2} = \frac{\rho_0 \cos \alpha g \beta (T_1 - T_0)}{2 a^u_{i,j-1/2}} \quad (9)$$

where the geometric coefficients F's can be interpreted as (area of flow)/(volume of computational node). Further, when calculating free-convection flows oriented as in Figure 1, the nondimensional temperature is defined as

$$\Theta = \frac{T - T_0}{T_1 - T_0} \quad (10)$$

and considers the maximum T drop across the computational domain, $\Delta T = (T_1 - T_0)$. The coefficients a_{nb}^{ϕ} appearing in Eqs. (5)–(7), referent to *neighbor nodal points*, accounts for the contributions, at each face, of the mechanisms of convection and diffusion. For the general variable ϕ and for the purely upwind formulation considered here, its general form reads

$$a_{nb}^{\phi} = \frac{\Gamma_{\phi}}{\rho} \frac{A_{nb}}{\delta r_{nb}} + \| A_{nb} U_{nb}, 0 \| \tag{11}$$

where A_{nb} is the area of transport, U_{nb} is the velocity prevailing over the control-volume face area A_{nb}, and δr_{nb} is the distance between adjacent control-volume centers. Also, in Eqs. (5)–(6), f signifies all sources except the pressure gradient and buoyancy terms. It is important to notice that the source term in (3) and (4) explicitly shows the contribution due to buoyancy. For the coupled treatment here presented, this arrangement is necessary, as will be seen below.

Numerical Strategy

In order to smooth out errors due to initial guessed fields, corrections are defined as differences between *exact* and *approximate* variables. Residuals for momentum equations at each control-volume face, and continuity of mass and energy equations are obtained by applying the just-defined approximate values into (3)–(4)–(7). After some manipulation, a system connecting the residuals and corrections of equations (2)–(3)–(4)–(7) can be written into matrix form as

$$\begin{bmatrix} 1 & 0 & 0 & 0 & \hat{d}_{i-1/2} & \hat{g}_{i-1/2} \\ 0 & 1 & 0 & 0 & -\hat{d}_{i+1/2} & \hat{g}_{i+1/2} \\ 0 & 0 & 1 & 0 & \hat{d}_{j-1/2} & \hat{g}_{j-1/2} \\ 0 & 0 & 0 & 1 & -\hat{d}_{j-1/2} & \hat{g}_{j+1/2} \\ -F_{i-1/2} & F_{i+1/2} & -F_{j-1/2} & F_{j+1/2} & 0 & 0 \\ 0 & 0 & 0 & 0 & 0 & 1 \end{bmatrix} \begin{bmatrix} U'_{i-1/2,j} \\ U'_{i+1/2,j} \\ W'_{i,j-1/2} \\ W'_{i,j+1/2} \\ P'_{i,j} \\ \Theta'_{i,j} \end{bmatrix}$$

$$= \begin{bmatrix} R_{i-1/2,j} \\ R_{i+1/2,j} \\ R_{i,j-1/2} \\ R_{i,j+1/2} \\ R_{i,j} \\ R^{\Theta}_{i,j} \end{bmatrix} \tag{12}$$

In Eq. (12) the four first rows correspond to discretized forms of momentum equations applied to the four faces of the control volume of Figure 1. The fifth row comes from the continuity equation and the last one has its origin in the

discretization of Eq. (7). Here also the subscripts identifies locations in the grid, the superscript ′ distinguishes corrections, and the left-hand-side residue vector corresponds to the one at the previous iteration. In Eq. (12) the influence of Θ on the flow field is directly accounted for by the g terms. The reverse effect—say, the cross-flow influence on temperature—is not treated implicitly. The solution of system (12) is easily obtained by finding first corrections for Θ and then calculating the pressure P and velocity components U and W.

Partially Segregated Treatment

The algebraic equations for the velocity field were solved, in addition to the fully coupled scheme described here, by performing outer iterations for the nondimensional temperature while keeping U–W–P from the previous iteration. A *line-by-line* smoothing operator, fully described elsewhere [8], was used to relax Θ, with the cross-flow field (U, W) calculated by the locally coupled method seen above. This *partially segregated* or *semicoupled* solution was set in such a way that the same number of sweeps per outer iteration, throughout the scalar (Θ) and cross-flow fields (U, W), was obtained in both the coupled and semicoupled methods. This procedure was found to be a reasonable way to compare the two methods.

The reason for recalling this second procedure a *partial* rather than a *full* segregation lies in the fact that in full segregated methods all variables, including U, W, and P, are solved independently and in sequence along the entire algorithm. In the case presented here for comparison, only Θ is excluded from the implicit treatment implied by Eq. (12).

Boundary Conditions and Computational Details

All velocity components were of null value at all boundaries. Interior velocities were also set to zero at the start. For temperature, Figure 1 illustrates that the left and right walls were assigned the nondimensional temperatures of +1 and 0, respectively. At the upper and bottom plates the isolation condition $\partial\Theta/\partial z = 0$ was applied. A single grid of several sizes and equally distributed in the domain was used. The same relaxation parameters ($\gamma_\phi = 0.40$ for $\phi = U, W, P, T$) were used in all calculations. The Rayleigh number, appearing after nondimensionalizing the buoyancy term, is given by $\mathrm{Ra} = (\rho^2 L^3 \mathbf{g} \beta \Delta T \, \mathrm{Pr})/\mu^2$, where, in all cases, the Prandtl number Pr was set equal to 1.0.

Also, an essential feature of Vanka's algorithm [11, 12], the multigrid technique, has not been used in the present study. Multigrid acceleration is known to be advantageous for mid- to large-size grids, but for the modest meshes analyzed here no substantial improvement on convergence rates was expected. Instead, a different domain sweep strategy was adopted. Distinct sweeping modes, namely horizontal and vertical, together with an alternating path in order to keep always physically connected cells, were followed when visiting each cell in the computational domain. For that, this sweeping strategy is here called *alternating symmetric coupled Gauss-Seidel* or ASCGS for short. A comparison between SGCS and ASCGS is shown in Figure 2.

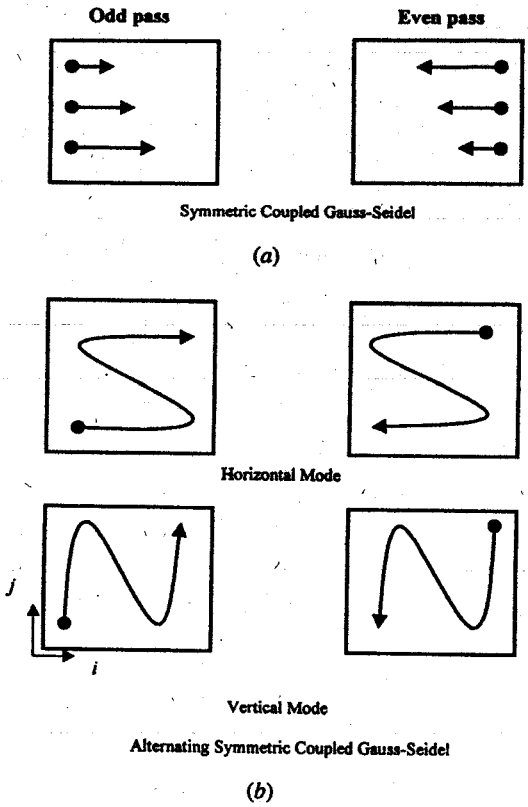

Figure 2. Different sweeping strategies: (*a*) SCGS, from node i, j to $i$max, $j$max and back; (*b*) ASCGS, subsequent lines or columns keep always physically connected cells in both horizontal and vertical sweeping modes.

RESULTS AND DISCUSSION

Preliminary Results

Although this work has not been concerned primarily with the accuracy of the solution (absolute value), but rather with the algorithm to achieve it, a few results on the velocity fields are presented here for completeness. These preliminary results ensure program validation and were taken after reduction of all normalized residues for mass, momentum, and energy equations to the preselected value of $1.\times 10^{-5}$. Residue history for the velocity calculations shown below are presented later in this article and are referent to as the HFB and VRT cases (see Table 1).

Grid independence studies were conducted in order to determine a suitable grid size for the calculations. For square horizontal cavities heated from below, computations with different grids are presented in Figure 3*a*. The figure shows results for the u-velocity at the chamber mid-plane for the HFB case ($y = L/2$, $\alpha = \pi/2$, $H/L = 1$, $\mathrm{Ra} = 4.\times 10^4$; see Figure 1 and Table 1). One can see that for meshes larger than 45×45 the solution is nearly grid independent. Absolute values for velocities in buoyancy-driven flow in cavities have also been compared with benchmark solutions [17] to check code accuracy and correctness [13–16].

The Nusselt number Nu and the film coefficient h for the enclosure are calculated as an average of the values prevailing at the *east* and *west* faces. The

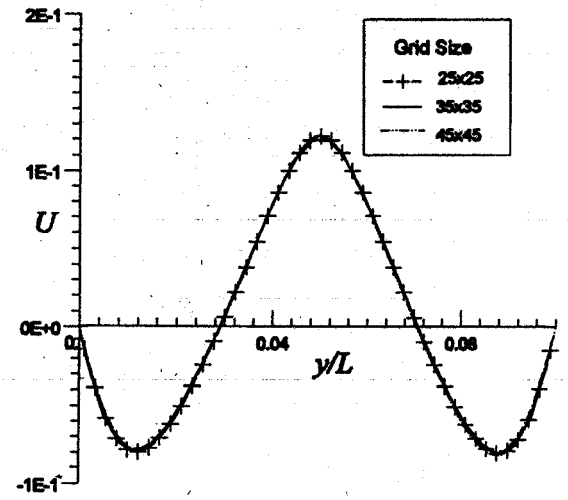

(a)

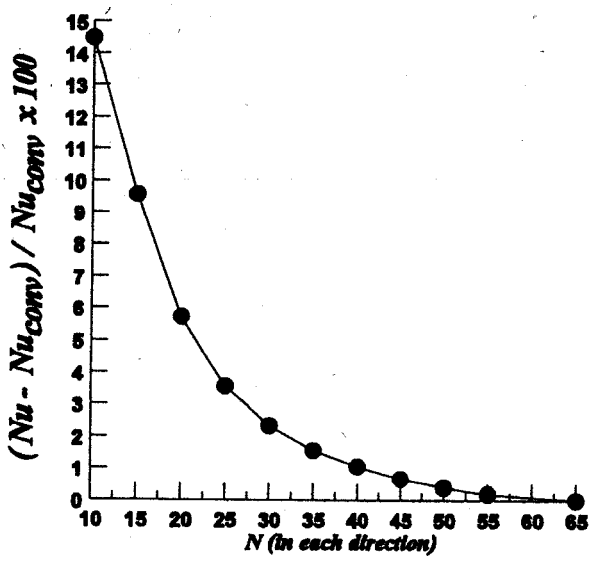

(b)

Figure 3. Grid independence studies: (*a*) vertical velocity component; (*b*) Nusselt number.

equations used were

$$\mathrm{Nu} = \frac{hL}{k} \qquad h = \frac{h_e + h_w}{2} \tag{13}$$

where e and w correspond to the nonisolated faces of the cavity shown in Figure 1 and k is the fluid thermal conductivity. For the face e or east,

$$h_e = \frac{\overline{q_e^{11}}}{\Delta T} \qquad \overline{q_e^{11}} = \frac{1}{A_e}\int_{A_e} q_e^{11}\, dA_e \qquad q_e^{11} = -k\left.\frac{\partial T}{\partial z}\right)_e \tag{14}$$

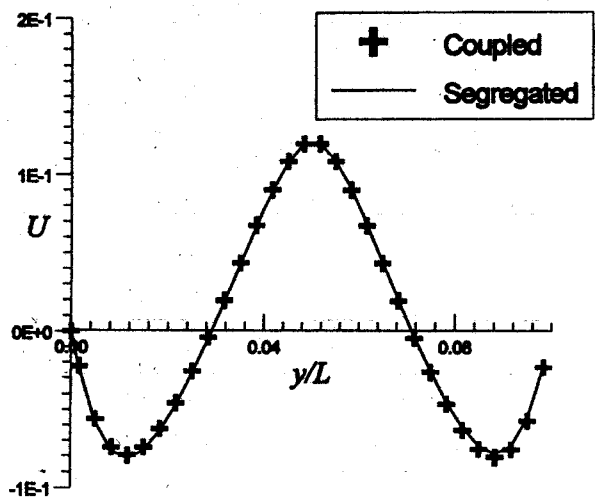

Figure 4. Comparison of partially segregated and coupled results.

Figure 3*b* presents results for Nu as a function of the number of grid points. Results are presented in terms of $(\mathrm{Nu} - \mathrm{Nu}_{\mathrm{conv}})/\mathrm{Nu}_{\mathrm{conv}} \times 100$, where the subscript "conv" refers to the asymptotic value as the grid increases. The figure indicates that for grids greater than 45×45, errors in Nu are less that 1%. For that, all results presented below considered this grid size. The absolute asymptotic value $\mathrm{Nu}_{\mathrm{conv}}$ calculated with Eqs. (13)–(14) for $\mathrm{Ra} = 4. \times 10^4$ and for the VRT case ($\alpha = 0$) was equal to 3.49. This value is only 0.85% higher than the one given by the correlation by Catton in 1978 [1]. In spite of the close agreement with the correlation, one should point out that the use of an upwind differencing scheme to model convective fluxes may have contaminated the solution with some numerical diffusion. Also, an equally distributed grid has been used and no grid layout optimization, known to improve results accuracy, has been made use of.

Figure 4 presents again the u-component for the same case and position as in the previous Figure 3*a*, but now comparing the results calculated by the *partially segregated* and *coupled* approaches. Inspecting the figure one can conclude that, independent of the error-smoothing technique used, final converged solutions are essentially equal, as expected. The computational effort to achieve them, however, seems to be different, as will be discussed later.

Effect of Ra

The influence of the Rayleigh number on the thermal and velocity fields is shown in Figure 5. For better visualization, streamlines are shown instead of vector plots. The simulation is concerned with the case of an enclosure heated from below (HFB case in Table 1) and with aspect ratio $H/L = 1$. For large aspect ratios ($H/L \to \infty$), the so-called *Bénard cells* are known to exist in the range $1{,}708 \leq \mathrm{Ra} \leq 50{,}000$. For compact enclosures, such as the one in question, the critical Ra for the onset of motion increases due to the drag of the side walls [2]. Consequently, less heat is transferred across the same layer thickness and Ra.

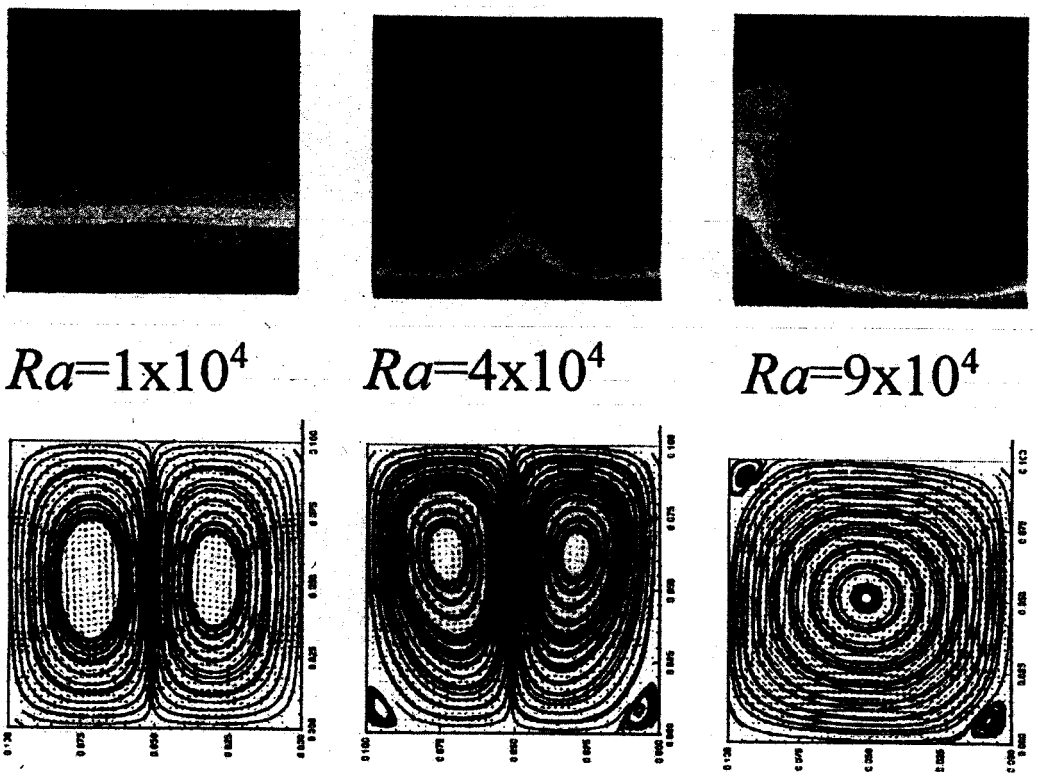

Figure 5. Effect of Ra on temperature and velocity fields—cavity heated from below (HFB).

Figure 5 shows that for small values of the Rayleigh number, only a slight departure from the purely conduction regime is detected, most likely due to the weak recirculation computed. As Ra increases to $4.\times 10^4$, the circulatory motion brings the bottom hot-temperature stream up to the top wall, substantially penetrating into the flow core. A further increase in Ra destroys the doubled-swirl pattern and the flow enters the transition regime. In the same figure the corresponding streamlines further show that at $Ra = 4.\times 10^4$ a small recirculation bubble appears attached symmetrically at the bottom corners. An increase in the value of Ra ($9.\times 10^4$) seems to reach the instability regime and, as can be seen, a single cell pattern is obtained. Further increases in Ra would lead to the turbulent regime, which cannot be computed with the mathematical model herein.

Figure 6 presents similar results for vertical enclosures or, say, when the overall heat transfer rate crosses from left to right, with both horizontal surfaces insulated (VRT case, $\alpha = 0$). Here also the figure shows a sequence of temperature and flow fields subjected to an increasing Rayleigh number. At low Ra (left), a small recirculating current distorts the temperature field, bringing the hotter temperature at the upper left corner into the cavity mid-plane. A further increase in Ra (2.8×10^5) enhances convective transport across the layer, increasing the strength of convection currents. At this stage, a larger recirculating bubble takes place over most of the flow core. Vertical stratification of temperature develops

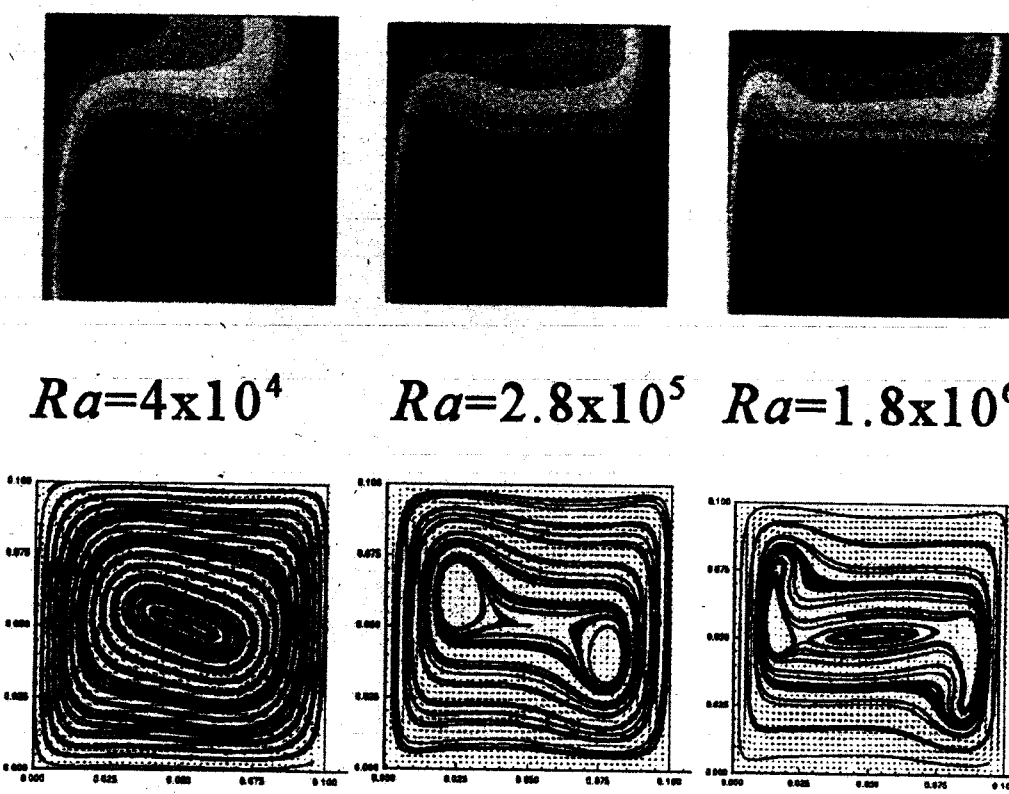

Figure 6. Temperature and velocity fields for cavity heated from left (VRT).

over that same region. At Ra = 1.8×10^6, the boundary-layer regime can be clearly detected. The temperature distribution in the core region reveals considerable stratification and the penetration of the wall layers near the horizontal plates are simulated correctly [3].

Effect of Aspect Ratio H/L

The effect of the aspect ratio H/L is shown in Figures 7 and 8 for a fixed Rayleigh number equal to $4. \times 10^4$ and H/L up to 4. The three flow regimes known in the literature [3]—namely, the boundary-layer type, the transition, and conduction regimes as H/L increases—are not fully simulated due to the relatively small Ra used and the narrow range for H/L. The solution for $H/L = 4$ seems to be a representative of the boundary-layer regime for this Ra, having a somewhat stratified core and a unicell flow structure. As the H/L ratio increases (not shown here), flow stratification prevails over most of the domain and the conduction mechanism controls heat transfer [3]. It is also interesting to note that as H/L increases, the major flow current changes from horizontal to vertical and the core of the flow becomes mostly stratified. Also, a reduction on the average temperature gradient at the wall, due to stratification, decreases the Nusselt number, ultimately leading to the mentioned conduction-dominated regime.

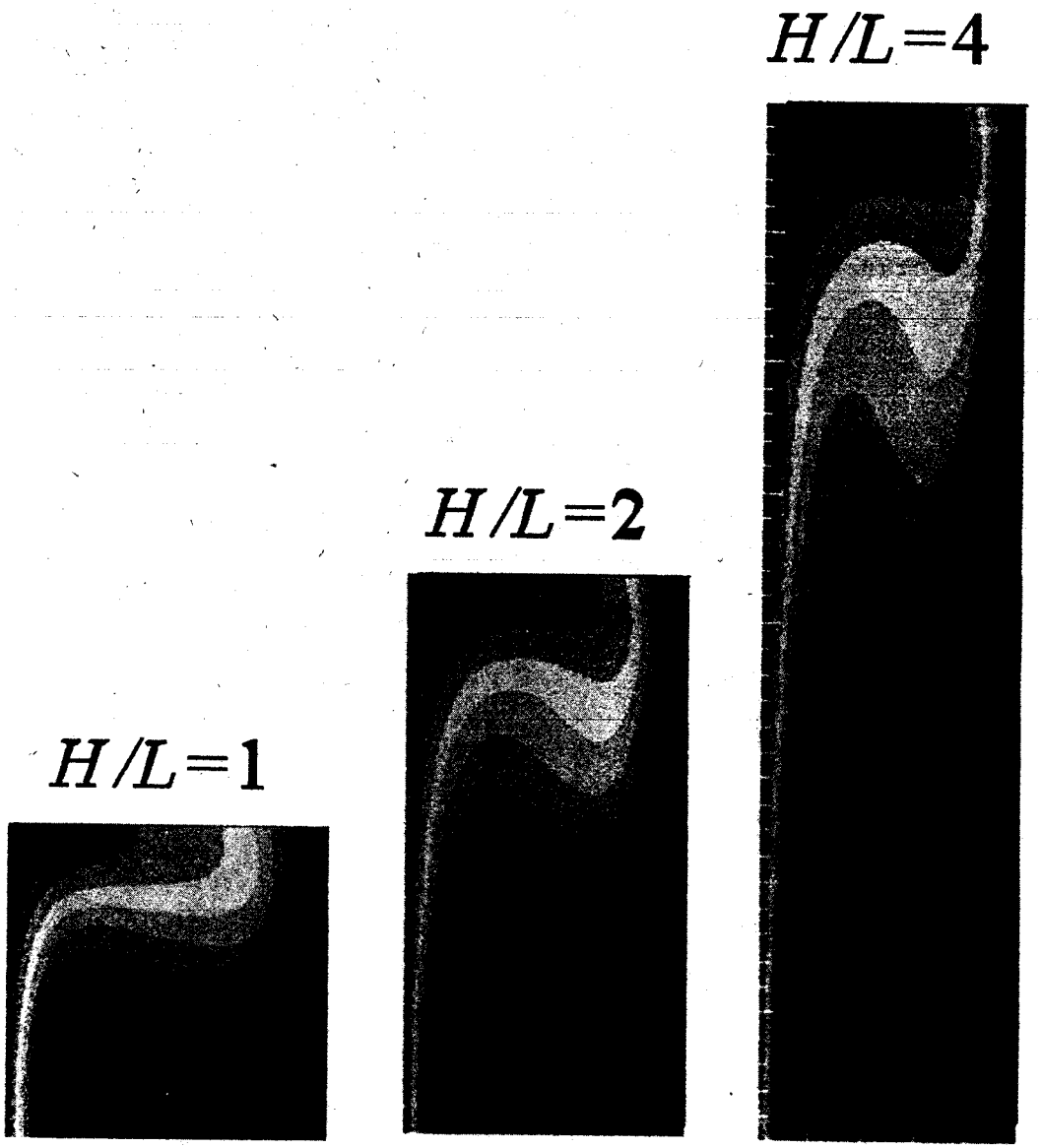

Figure 7. Effect of H/L on temperature for vertical cavity heated from left.

Effect of Tilt Angle α

Isotherms as a function of the tilt angle and for $Ra = 4 \times 10^4$ are shown in Figure 9. For the HFB case (*upper left corner*), one can clearly see the bulging of the isolines deeply penetrating into the flow core. The circulatory motion provoking that is illustrated in Figure 10 and is akin to the Bénard cells flow structure. Also interesting to note is the small recirculating bubble at the bottom of the cavity in Figure 10 (see same case in Figure 5). Returning to Figure 9, one can also see temperature fields for the tilt angle α spanning from an unconditionally unstable

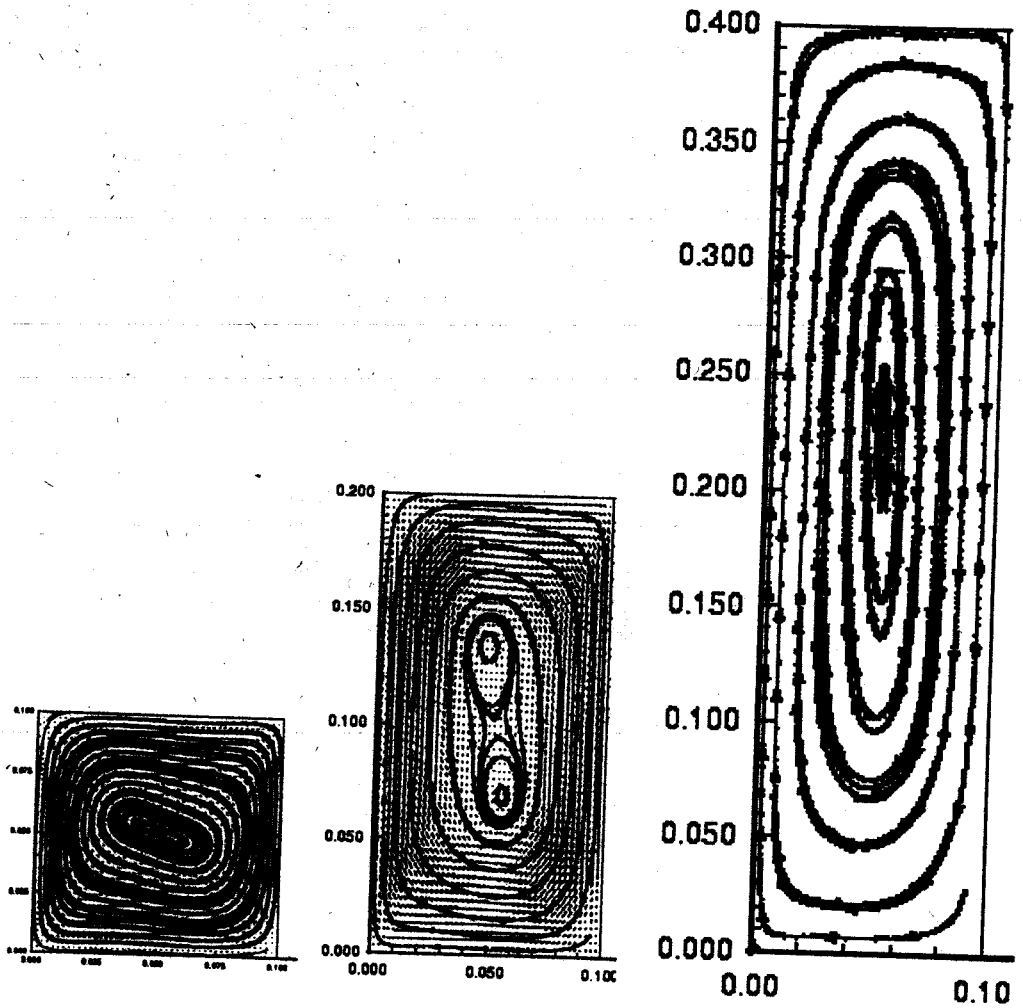

Figure 8. Streamlines for different aspect rations for vertical cavities.

situation (HFB, $\alpha = 90°$) to stable no-flow distribution (HFA, $\alpha = -90°$). These results are in agreement with pertinent literature and indicate the correctness of the computer program developed.

Residues

Normalized residue was defined as the norm of the cell mass and energy equation residues as

$$R_{\text{abs}} = \left(\frac{\Sigma_{ij} R_{ij}^2}{N \cdot M} \right)^{1/2} \qquad R_T = \left(\frac{\Sigma_{ij} \left(R_{ij}^{\Theta} \right)^2}{N \cdot M} \right)^{1/2} \tag{15}$$

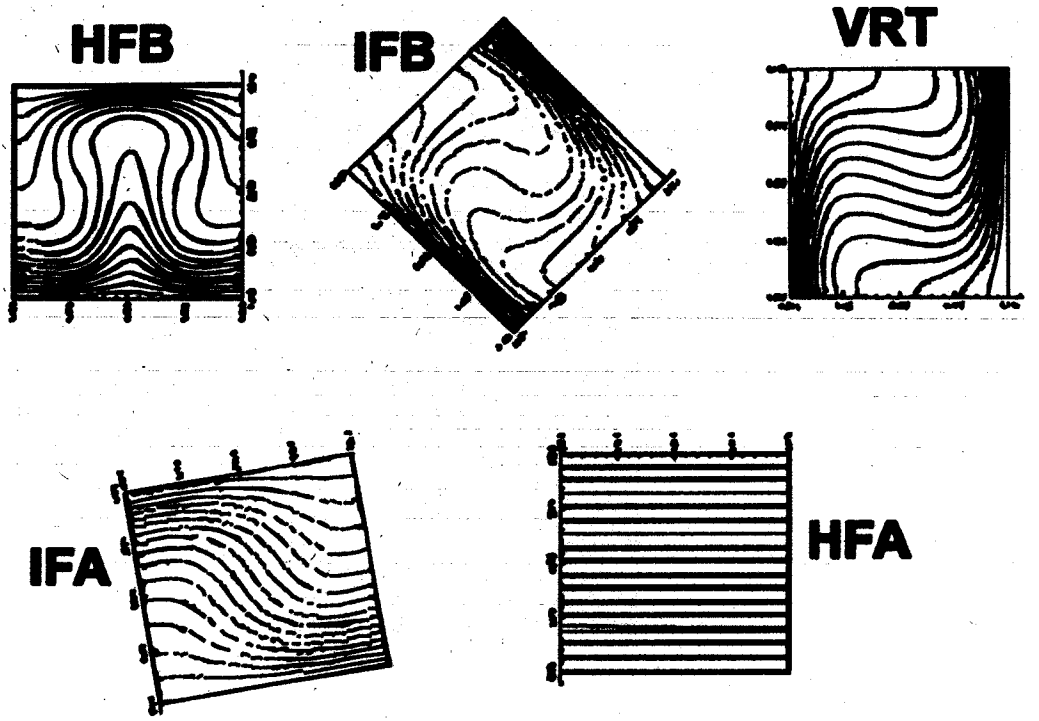

Figure 9. Isotherms for different cavity inclinations: HFB, $\alpha = 90°$; IFB, $\alpha = 45°$; VRT, $\alpha = 0°$; IFA, $\alpha = -85°$; HFA, $\alpha = -90°$.

where N and M are the number of cells in the y and z directions, respectively, and $R_{i,j}$ can be seen as the difference, for every cell, between the cell *outgoing* mass flux, F_{out}, and the *incoming* mass flux, F_{in}. Further, R_T in (15) is the residue for the energy equation (7).

A *relative* mass residue can also be defined as

$$R_{\text{rel}} = \left[\frac{\Sigma_{ij} \left(\dfrac{F_{\text{in}} - F_{\text{out}}}{F_{\text{in}} + F_{\text{out}}} \right)^2}{N \cdot M} \right]^{1/2} \tag{16}$$

A discussion of the advantages in simultaneously monitoring R_{rel} in addition to R_{abs} is presented in [13–16], based on the small range of the former (0, +1).

Mass residues for the HFB case calculated by Eqs. (15) and (16) are presented in Figure 11. The iteration counter refers to the total number of sweeps over the domain, that is, the product of the *outer* counter times the number of *inner* sweeps. Here, a quick word on the number of iterations to convergence seems timely. Other schemes presented in the literature may indicate residue

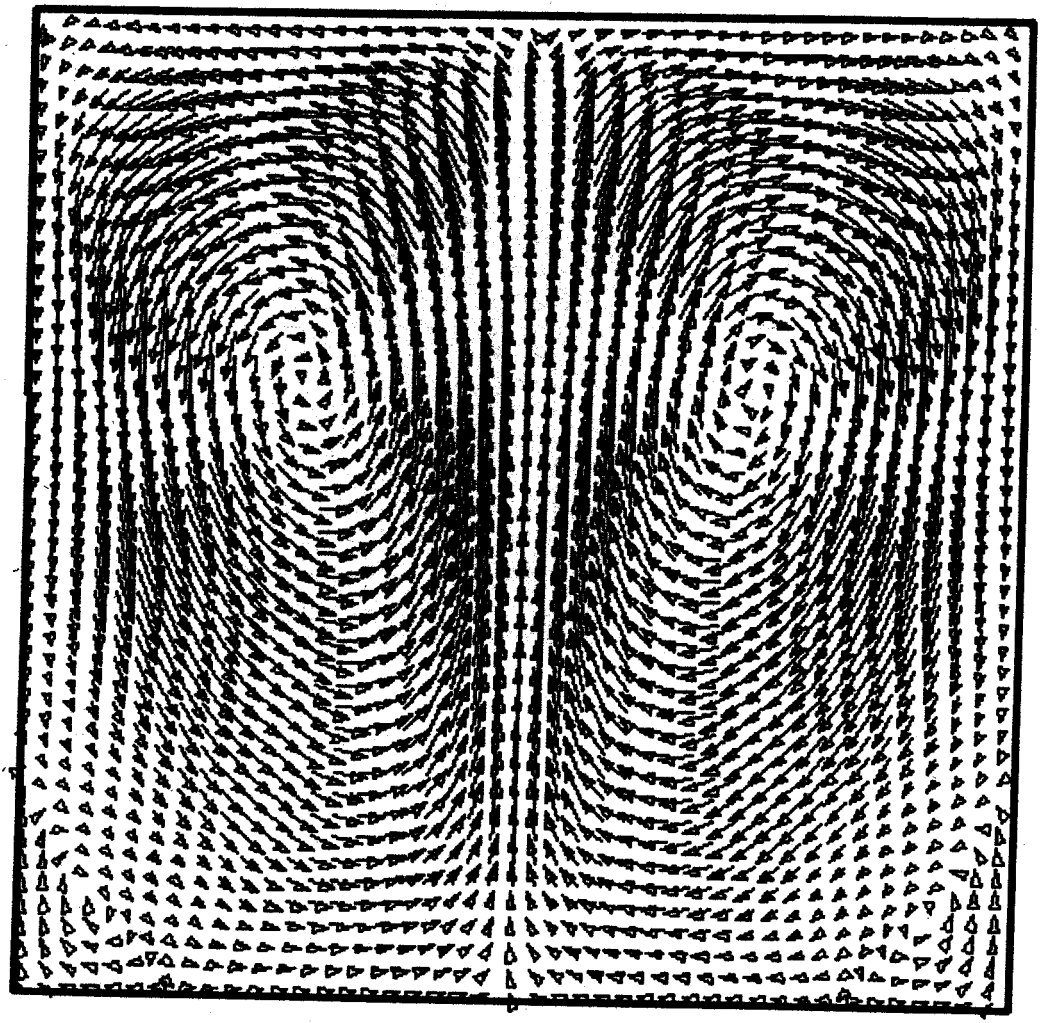

Figure 10. Vector plot for HFB case, $\alpha = 90°$.

history as a function of *outer* iteration counters only. Some use the so-called *pseudo-transient* approach and plot *time steps* instead. Each outer iteration, in turn, may consider a great number of internal sweeps, usually controlled by a specified residue reduction rate. Here, in this work, a fixed number of internal sweeps was considered. The relatively large number of necessary iterations seen in the figures below could be associated with the use of a single grid, the tightness of the relaxation parameters, and the strong coupling among all variables involved.

Figure 11*a* indicates that, after an initial period of about 6,000 overall iterations, a better convergence rate is obtained with the coupled scheme in either residue form. For Eq. (7), the residue R_T is presented in Fig. 11*b*, here also comparing the performance of both relaxation procedures. It is noteworthy that, although Figures 11*a*–11*b* correspond to the same case (HFB), they consider

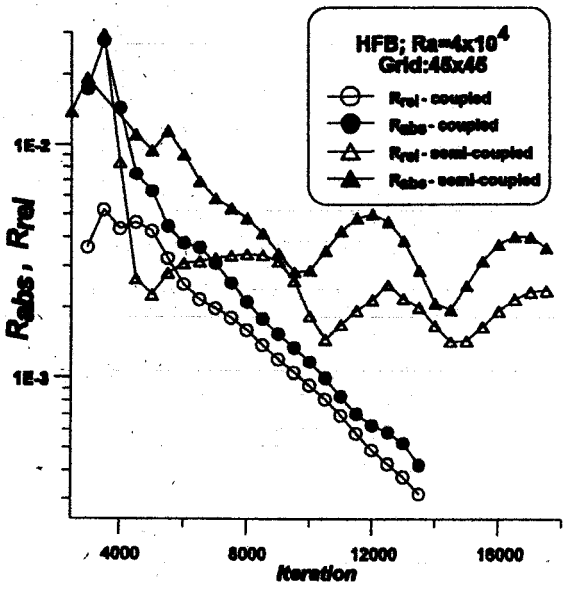

(*a*)

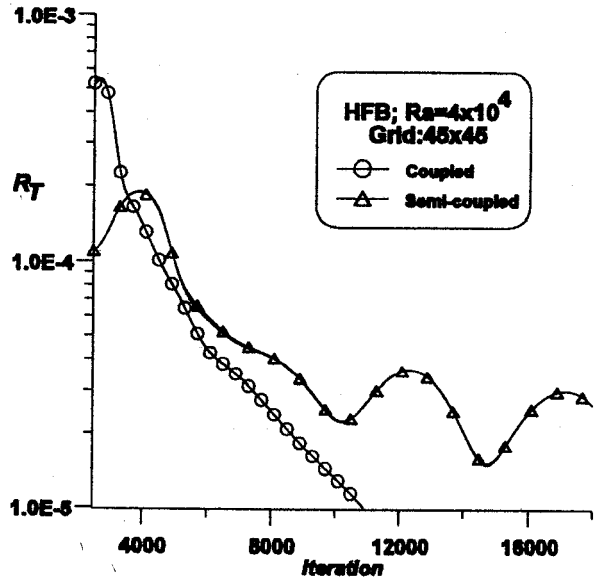

(*b*)

Figure 11. Residue history for HFB case: (*a*) relative and absolute mass residues; (*b*) residue for energy equation.

different independent variables requiring a different number of iterations to reduce the residue to the same preselected level. For temperature, 4,000 iterations after the beginning of the relaxation suffice for detecting the advantages of the coupled scheme.

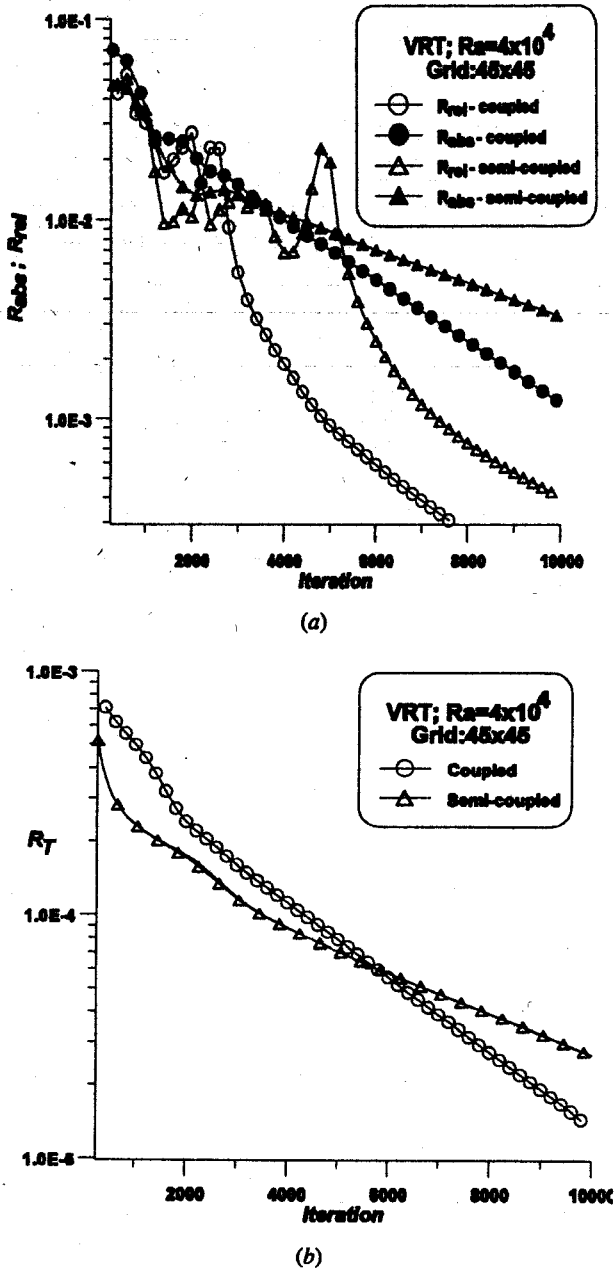

Figure 12. Residue history for VRT case: (*a*) mass residue; (*b*) energy equation residue.

Finally, Figure 12 shows similar results for the vertical cavity case, where heat flows from left to right. The advantages of using a coupled scheme, rather than relaxing temperature separately, is clear in the figures. Both mass residues, in absolute and relative formats, show better performance for around 3,000 iterations in Figure 12*a*. The apparent advantage of the semicoupled procedure over the

coupled algorithm shown on the left of Figure 12*b*, lasts only up to 6,000 iterations. After that, changes in the temperature field are quickly transferred to the cross-flow, which, in turn, mixes temperature at a faster rate and brings R_T down to the preselected tolerance.

CONCLUDING REMARKS

This article detailed a fully coupled technique for numerical prediction of the thermal and flow field in enclosures heated from below and at the left. The discretized momentum equations are applied to each cell face and then, together with the mass-continuity, tangential velocity, and energy equations, are solved directly in each computational node. Robustness of the proposed implicit method avoids divergence when calculating flows with such high degree of coupling. Finally, it is also expected that more advanced parallel computer architectures can benefit from the error-smoothing operator described here.

REFERENCES

1. I. Catton, Natural Convection in Enclosures, *Proc. 6th. Int. Heat Transfer Conf.*, Toronto, Canada, vol. 6, p. 13, 1978.
2. S. Churchill, Free Convection in Layers and Enclosures, in E. U. Shlünder (ed.), *Heat Exchanger Design Handbook*, Section 2.58, Hemisphere Publishing, New York, 1983.
3. K. T. Yang, Natural Convection In Enclosures, in S. Kakaç, R. K. Shah, and W. Aung (eds.), *Handbook of Single Phase Convective Heat Transfer*, chap. 13, 1987.
4. K. G. T. Hollands, T. E. Unny, G. D. Raithby, and L. Konicek, Free Convection Heat Transfer across Inclined Air Layers, *J. Heat Transfer*, vol. 98, pp. 189–193, 1976.
5. G. de Vahl Davis, Natural Convention of Air in a Square Cavity: A Bench Mark Numerical Solution, *Int. J. Numer. Meth. Fluids*, vol. 3, pp. 249–264, 1983.
6. G. de Vahl Davis and I. P. Jones, Natural Convention of Air in a Square Cavity: A Bench Mark Numerical Solution, *Int. J. Numer. Meth. Fluids*, vol. 3, pp. 227–2248, 1983.
7. M. Hortmann, M. Periç, and G. Scheider, Finite Volume Multigrid Predictions of Laminar Natural Convection: Benchmark Solutions, *Int. J. Numer. Meth. Fluids*, vol. 11, pp. 189–207, 1990.
8. S. V. Patankar, *Numerical Heat Transfer and Fluid Flow*, McGraw-Hill, New York, 1980.
9. P. F. Galpin and G. D. Raithby, Numerical Solution of Problems in Incompressible Flow: Treatment of the Temperature-Velocity Coupling, *Numer. Heat Transfer*, vol. 9, pp. 105–129, 1986.
10. L. Tang and Y. K. Joshi, Application of Block Implicit Multigrid Approach to Three-Dimensional Heat Transfer Problems Involving Discrete Heating, *Numer. Heat Transfer A*, vol. 35, pp. 717–734, 1999.
11. S. P. Vanka, Block-Implicit Multigrid Solution of Navier-Stokes Equations in Primitive Variables, *J. Comput. Phys.*, vol. 65, pp. 138–158, 1986.
12. S. P. Vanka, A Calculation Procedure for Three-Dimensional Steady Recirculating Flows Using Multigrid Methods, *Comput. Meth. Appl. Mech. Eng.*, vol. 55, pp. 321–338, 1986.
13. M. J. S. de Lemos, Computation of Laminar Axi-Symmetric Recirculating Flows Using Primitive Variables and a Block-Implicit Scheme, *Proc. ENCIT90—3rd Brazilian Thermal Sciences Meeting*, vol. 1, pp. 375–380, Itapema, SC, Brazil, 10–12 December 1990.

14. M. J. S. de Lemos, Computation of Buoyancy-Driven Flows Using a Block-Implicit Numerical Scheme, *Proc. 28th Natl. Heat Transfer Conf.*, vol. ASME-HTD-194, pp. 83–89, San Diego, CA, USA, 9–12 August 1992.
15. M. J. S. de Lemos, Locally-Coupled Numerical Solution of Thermally-Driven Cavity Flows, *Proc. COBEM97—14th Brazilian Congress of Mechanical Engineering* (on CD-ROM), Bauru, São Paulo, Brazil, 8–12 December 1997.
16. M. J. S. de Lemos, Cell-Implicit Numerical Computation of Flow Field and Heat Transfer in Inclined Cavities, *Proc. COBEM97—14th Brazilian Congress of Mechanical Engineering* (on CD-ROM), Bauru, São Paulo, Brazil, 8–12 December 1997.